Photofragment translation spectroscopy of ClN_3 at 248 nm: Determination of the primary and secondary dissociation pathways

N. Hansen[a),b)]
Department of Chemistry and Biochemistry, University of California, Santa Barbara, California 93106 and Combustion Research Facility, Sandia National Laboratories, Livermore, California 94551

A. M. Wodtke[a),c)]
Department of Chemistry and Biochemistry, University of California, Santa Barbara, California 93106

S. J. Goncher, J. C. Robinson,[d)] N. E. Sveum, and D. M. Neumark
Department of Chemistry, University of California, Berkeley, California 94720 and Chemical Sciences Division, Lawrence Berkeley National Laboratory, Berkeley, California 94720

(Received 20 April 2005; accepted 17 May 2005; published online 12 September 2005)

Photofragmentation translational spectroscopy was used to identify the primary and secondary reaction pathways in the KrF laser (248 nm) photodissociation of chlorine azide (ClN_3) under collision-free conditions. Both the molecular channel producing NCl ($X\,^3\Sigma, a\,^1\Delta$)+N_2 and the radical channel producing Cl (^2P_J)+N_3 were analyzed in detail. Consistent with previously reported velocity map ion imaging experiments [N. Hansen and A. M. Wodtke, J. Phys. Chem. A **107**, 10608 (2003)] a bimodal translational energy distribution is seen when Cl atoms are monitored at $m/z=35(Cl^+)$. Momentum-matched N_3 counterfragments can be seen at $m/z=42(N_3^+)$. The characteristics of the observed radical-channel data reflect the formation of linear azide radical and another *high-energy form* of N_3 (HEF-N_3) that exhibits many of the characteristics one would expect from cyclic N_3. HEF-N_3 can be directly detected by electron-impact ionization more than 100 μs after its formation. Products of the unimolecular dissociation of HEF-N_3 are observed in the $m/z=14(N^+)$ and $m/z=28(N_2^+)$ data. Anisotropy parameters were determined for the primary channels to be $\beta=-0.3$ for the NCl forming channel and $\beta=1.7$ and $\beta=0.4$ for the linear N_3 and HEF-N_3 forming channels, respectively. There is additional evidence for secondary photodissociation of N_3 and of NCl. © *2005 American Institute of Physics*. [DOI: 10.1063/1.1948381]

INTRODUCTION

This paper springs from our continuing interest in the rich UV photodissociation dynamics of chlorine azide (ClN_3).[1–5] Primary photoproducts are formed in a molecular elimination channel,

$$ClN_3 + h\nu \rightarrow NCl(a\,^1\Delta) + N_2(X\,^1\Sigma_g^+), \tag{1a}$$

$$ClN_3 + h\nu \rightarrow NCl(X\,^3\Sigma) + N_2(X\,^1\Sigma_g^+), \tag{1b}$$

or in a radical-forming bond-rupture channel

$$ClN_3 + h\nu \rightarrow Cl(^2P_J) + N_3(X\,^2\Pi). \tag{2a}$$

Historically, interest in the photochemistry of ClN_3 (Refs. 6–13) derived from the utility of one of its photoproducts, NCl($a\,^1\Delta$), as an effective energy carrier in an all gas-phase chemical iodine laser (AGIL).[14–18]

More recently, the ClN_3 photochemistry has received considerable attention due to its potential use as a possible photolytic precursor of cyclic N_3. Hansen and Wodtke reported velocity map ion imaging experiments of ClN_3 photodissociation at 235 nm under collision-free conditions and showed that the translational energy distribution of the Cl fragment is bimodal.[1] This observation indicates that, in addition to the formation of the well-known linear N_3 (azide radical), the radical channel also leads to the formation of a *high-energy form* of the N_3 molecule hereafter referred to as HEF-N_3. It was pointed out that the maximum translational energy release of reaction,

$$ClN_3 + h\nu \rightarrow Cl(^2P_J) + \text{HEF-}N_3, \tag{2b}$$

could be used to extract a heat of formation that was in excellent agreement with theoretical predictions of the heat of formation of the cyclic-N_3 isomer.

Although it is yet to be definitively proven that cyclic N_3 is a primary product of ClN_3 photochemistry, its predicted properties are quite interesting and represent a significant motivation for the present study. Briefly, cyclic N_3 is a Jahn-Teller molecule that exhibits a conical intersection at the D_{3h} (equilateral triangle) configuration. This conical intersection must distort to form one of the three equivalent C_{2v} minima. The barrier to interconversion between equivalent C_{2v} minima (pseudorotation) is comparable to the zero-point vibrational energy. The vibrationless state of N_3 is doubly degenerate, delocalized between minima, and lies ~9 kcal/mol below the conical intersection.[19] A recent paper[20] has shown that cyclic N_3 is ideal for the study of the geometric phase effect[21,22] (Berry's phase) in molecules. The geometric phase

[a)]Authors to whom correspondence should be addressed.
[b)]Electronic mail: nhansen@sandia.gov
[c)]Electronic mail: wodtke@chem.ucsb.edu
[d)]Present address: Intel Corporation, Hillsboro, OR 97124.

effect introduces "correction" factors in determining the energies of the vibrational states in this molecule, which are predicted to be on the order of 10^2 cm^{-1}. Furthermore, without correct consideration of the geometric phase effect, one cannot obtain accurate vibrational wave functions. Even the correct symmetry of the ground vibrational state (E) is incorrectly predicted to be A_1 if Berry's phase is neglected.[20] Experimental studies on the spectroscopy of cyclic N_3 would be very useful in extending our understanding of these phenomena in molecular systems.

What we know about HEF-N_3 has been learned from a few experiments and comparisons to theoretical work on cyclic N_3.[1,4,5,19,20,23–25] The experimentally observed excitation energy $\Delta E = 31 \pm 2$ kcal/mol is in very good agreement with recent *ab initio* calculations, which predicted the existence of a stable cyclic-N_3 isomer at an energy of 30.0 kcal/mol above the energy of the linear-N_3 isomer.[1,23] Recently, Samartzis *et al.* observed distinct ionization thresholds for the two forms of N_3.[5] Their experimental value IP (HEF-N_3) $= 10.7 \pm 0.2$ eV agrees well with the theoretically predicted value for cyclic N_3 of 10.58 eV.[24]

Babikov *et al.* presented a sophisticated adiabatic ground electronic state potential-energy surface which is constructed based on extensive high-level *ab initio* calculations.[19] Theory shows that cyclic N_3 is metastable with respect to the spin-forbidden dissociation,[19,25]

$$\text{cyclic } N_3(^2B_1) \rightarrow N(^4S) + N_2(X\ ^1\Sigma_g^+)$$
$$\Delta E \sim -32.3 \text{ kcal/mol}. \quad (3)$$

In addition, it is known that the doublet-quartet surface crossings that, when traversed, lead to dissociation lie about 28 kcal/mol above the cyclic-N_3 minimum.[25] Thus, while cyclic N_3 is metastable, it is thought to be long lived and, as it carries a great deal of chemical energy, it is an excellent new candidate for technological applications in energy storage, high nitrogen explosives, and clean propellants.

Other experiments have provided essential information needed to evaluate the photochemistry of ClN_3. Velocity map ion imaging of ClN_3 photoproducts was used to investigate the dissociative photoionization of ClN_3 under collision-free conditions,

$$ClN_3 + 2h\nu \rightarrow ClN_3^+ + e^- \rightarrow NCl^+ + N_2(X\ ^1\Sigma_g^+) + e^-, \quad (4)$$

which was observed by recording velocity map images of NCl^+ as well as state-selected N_2.[3] In another experiment, the molecular channel (1) was observed via velocity map images of state-selected N_2.[2] These two pieces of work provided accurate thermochemistry for reaction (1): $\Delta E = +4.8 \pm 1.8$ and -21.4 ± 2.1 kcal/mol for the decomposition of ClN_3 into $N_2(X\ ^1\Sigma_g^+) + NCl(a\ ^1\Delta)$ and $NCl(X\ ^3\Sigma)$, respectively. A comprehensive reevaluation of the thermochemistry of all molecules containing a single Cl atom and three N atoms including all new data from velocity map imaging has been reported.[1] All of the above experiments agree well with literature values for the 0 K heats of formation of $N_3(X\ ^2\Pi)$ and ClN_3.[26–28] The known dissociation energies of Cl–N_3 and of NCl ($a\ ^1\Delta, X\ ^3\Sigma$) are also in agreement with the new experiments.[29,30] All derived thermodynamic results were presented in Ref. 1 and will be helpful in the analysis of this work. Figure 1 summarizes the derived energy levels of the Cl–N–N–N system and shows the calculated barriers for dissociation of linear and cyclic N_3 into $N_2 + N(^4S, ^2D)$.

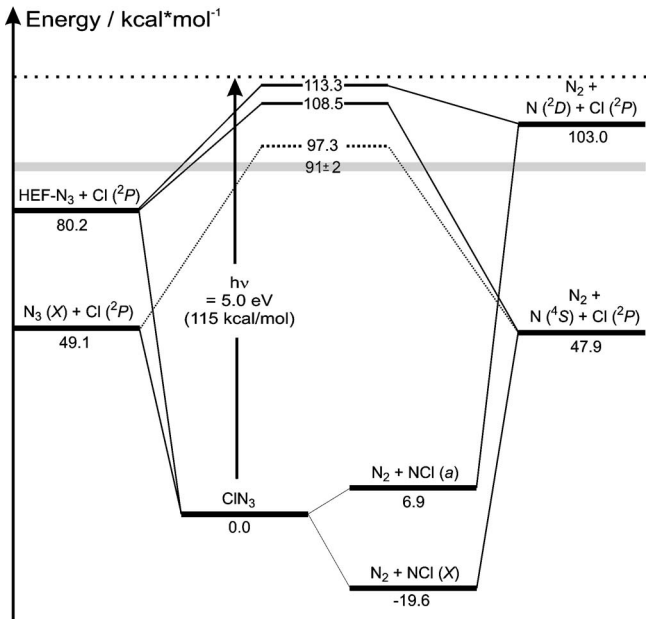

FIG. 1. Energy-level diagram for the Cl–N–N–N system relative to ClN_3. The energies of the N_3+Cl, the N_2+NCl, and the N_2+N+Cl levels are taken from Ref. 1. Also shown are the calculated lowest-energy barriers for dissociation of linear and cyclic N_3 into $N_2 + N(^2D, ^4S)$—for details see Ref. 25. The observed threshold for unimolecular dissociation of HEF-N_3 is shown as a gray bar.

Recently, molecular-beam photofragment translational spectroscopy (PTS) was applied to investigate the ClN_3 photodissociation dynamics at 248 nm under collision-free conditions. Using electron-impact (EI) ionization with quadrupole mass spectrometry enabled us to observe all channels simultaneously. In a previous letter we reported that the molecular dissociation channel, that is reaction (1), converts available energy predominantly into product internal excitation and that the branching ratio between the molecular elimination (1) and radical bond-rupture (2) channels was found to be $NCl + N_2/Cl + N_3 = 0.05 \pm 0.03/0.95 \pm 0.03$,[4] contrary to previous results that assumed $NCl + N_2$ to be the dominant channel.[11] As in the earlier imaging experiments,[1] a bimodal translational energy distribution was reported for the Cl atom in the PTS experiment.

In this paper, we describe a thorough analysis of the PTS experiments. In addition to the Cl and NCl data which were partially discussed in the previous letter, we now include data from N_3 photofragments as well as from N_2 and N fragments formed in secondary dissociation reactions. We show that HEF-N_3 can be detected by EI more than 100 μs after its formation. Specifically, we see that the N_3 photofragments exhibit a bimodal translational energy distribution that is consistent with momentum-matched Cl photofragments and the results from velocity map imaging. In addition, the angular distribution of the fast N_3 (linear azide) matches that of the fast Cl. Likewise, the angular distribution of the HEF-N_3 matches that of the slow Cl. A complete analysis of second-

ary dissociation pathways was carried out. This analysis shows that HEF-N_3 undergoes unimolecular dissociation forming both $N(^2D)+N_2$ and $N(^4S)+N_2$. In addition, secondary photodissociation of N_3 is seen, as is secondary photodissociation of NCl. We also conclude that unimolecular decomposition of energized NCl can be ruled out as a source of the slow Cl fragments.

Overall, these experiments now reveal the full set of microscopic collision-free decomposition pathways of ClN_3 resulting from photodissociation at 248 nm. The results provide a much firmer footing for the analysis of ClN_3 photolysis and add weight to previous conclusions concerning the possible photolytic production of cyclic N_3.

EXPERIMENT

The molecular-beam photodissociation instrument on which these experiments were performed has been described in detail previously.[31,32] A mixture of ClN_3 seeded in He carrier gas was prepared by passing a mixture of 10% Cl_2 in He over moist sodium azide (NaN_3). The NaN_3 was suspended in cotton wool and excess water was removed by passing the mixture through a drying agent (Drierite). Under normal operating conditions, mass spectral analysis of the beam showed NCl^+, an ionizer-induced fragment of ClN_3^+, and little or no Cl_2^+. When Cl_2^+ signal could be detected, the NaN_3 sample was replaced.

Using a backing pressure of ~0.5 bar, a pulsed molecular beam was formed by expanding the ClN_3/He mixture into vacuum through a piezoelectrically actuated pulsed valve.[33] After passing through two collimating skimmers, the molecular beam intersected a 28 ns pulsed beam of unpolarized 248 nm laser light produced by a Lambda Physik KrF excimer laser. Both the valve and the laser were operating at 100 Hz. The laser output (~72 mJ energy/pulse) was focused to a ~10 mm^2 spot at the region of intersection.

Photofragments scattered in the plane of the molecular laser beam were detected as a function of laboratory scattering angle, Θ with a rotatable, triply differentially pumped mass spectrometer. After passing through three collimating apertures, the photofragments were ionized by electron impact, mass selected with a quadrupole mass filter, and detected with a Daly-style detector. At various scattering angles, $\Theta=10°$–$60°$ in 10° steps, photofragment time-of-flight (TOF) distributions were taken for ions at selected mass-to-charge ratios, $m/z=35(Cl^+), 49(NCl^+), 42(N_3^+)$, $28(N_2^+)$, and $14(N^+)$, using a multichannel scaler interfaced to a personal computer. The velocity distribution of the parent ClN_3 molecular beam was characterized by TOF at $\Theta=0°$ using a retractable slotted chopper wheel to modulate the molecular beam.

TOF spectra obtained in this fashion were fitted by either the PHOTRAN (Ref. 34) or ANALMAX (Ref. 35) forward-convolution program. Both programs simulate the TOF spectrum based on "guessed" center-of-mass translational energy $[P(E_T)]$ distributions that are iteratively improved until a satisfactory fit to the data is obtained. Beam velocity, laboratory angle, dissociation and ionization volumes, finite angular acceptance angle of the detector, laser power, and polarization are additional program parameters used in the forward convolution.

RESULTS AND ANALYSIS

This section of the paper is organized as follows. First, the results from primary photodissociation processes are discussed. In particular, the analysis of the $m/z=49(NCl^+)$ TOF spectra is presented first, showing the energy release of reaction (1). Because the energy distribution of the N_2 counterfragments is complicated by secondary unimolecular dissociation and photodissociation processes of N_3, its analysis is presented later. In the second stage of presentation, we analyze the radical channel—in particular, the observed translational energy distribution of the Cl fragments. We then move on to an analysis of the $m/z=42(N_3^+)$ TOF, which exhibits the N_3 counterfragments to Cl in the radical channel. Finally the secondary processes are presented. Analysis of $m/z=28(N_2^+)$ and $m/z=14(N^+)$ leads to information on the unimolecular decomposition of N_3 and to evidence that the HEF-N_3 can be photodissociated at 248 nm. As part of the $m/z=35(Cl^+)$ TOF analysis, secondary NCl photodissociation is seen.

Molecular channel NCl+N_2

Observed TOF spectra of the NCl fragments ($m/z=49$) originating from reaction (1) are shown in Fig. 2 at several scattering angles, Θ. The data are represented by the open circles, while the solid lines are the results of forward-convolution simulations of the experiment using an optimized center-of-mass translational energy distribution shown in Fig. 3.

The best fit to the experimental data shown in Fig. 2 was obtained using the translational energy distribution shown in Fig. 3 and an anisotropy parameters of $\beta=-0.3$. The derived translational energy distribution shown in Fig. 3 is in good agreement with the previously reported distribution.[4] Owing to the non-state-selective detection scheme used in this experiment, identification of the electronic state of the NCl product, i.e., evaluating the relative importance of reactions (1a) and (1b), is not possible, although previous studies provided evidence that the spin-allowed reaction (1a) is more probable than reaction (1b).[11]

Besides reaction (1), other pathways, including the production of NCl ($X\,^3\Sigma$) via a spin-allowed channel,

$$ClN_3 + h\nu \rightarrow NCl(X\,^3\Sigma) + N_2(A\,^3\Sigma_g^+) \quad (5)$$

come into consideration. While this channel is not energetically accessible for 248-nm photolysis, when the photolysis wavelength is 193 nm, $N_2(A\,^3\Sigma_g^+)$, presumably from channel 5, has been detected,[6,12] along with NCl ($b\,^1\Sigma^+$) which can be produced by a second spin-allowed channel,[6,36]

$$ClN_3 + h\nu \rightarrow NCl(b\,^1\Sigma^+) + N_2(X\,^1\Sigma_g^+). \quad (6)$$

Coombe *et al.* reported that channels (5) and (6) amount to only ~1% of the 193 nm photolysis products.[12] Komissarov *et al.* estimated that ~1% of NCl is formed in the $b\,^1\Sigma^+$ state after ClN_3 photolysis at $\lambda=248$ nm.[11] $N_2(A\,^3\Sigma_g^+)$ lies ~6.2 eV above the ground-state $N_2(X\,^1\Sigma_g^+)$ and therefore is

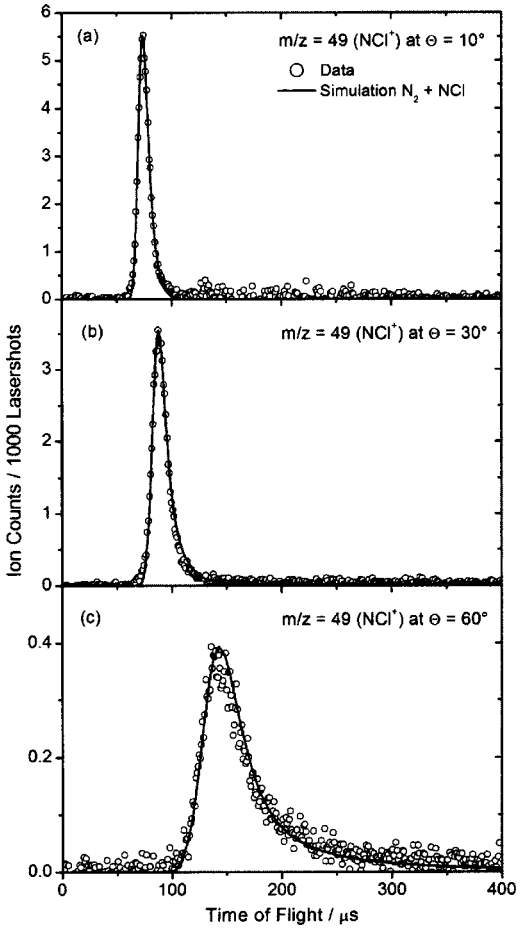

FIG. 2. Time-of-flight (TOF) spectra of $m/z=49(NCl^+)$ at detection angles $\Theta=10°$, 30°, and 60°. For all spectra the open circles represent the data. The solid line represents the forward-convolution fit to the data using the $P(E_T)$ distribution shown in Fig. 3.

not accessible by photolysis at $\lambda=248$ nm. Consequently, reactions (5) and (6) are not considered likely candidates to explain the data of Fig. 2.

According to recent experimental and theoretical work, the maximum available translational energy release is $E_{\max,NCl(a)}=108$ kcal/mol and $E_{\max,NCl(X)}=135$ kcal/mol for channels (1a) and (1b), respectively.[1,4] These values are substantially larger than the observed maximum translational energy release of ~48 kcal/mol (see Fig. 3). This means that the primary products, N_2 and NCl, are formed with a considerable amount of internal energy. This strong tendency to channel available energy into internal energy of the fragments has been postulated before on the basis of indirect kinetic evidence[4,8] and it is the most important feature of reaction (1). Indeed more than 70 kcal/mol goes to excite the internal degrees of freedom of the two diatomic products.

Radical-channel $Cl+N_3$

Cl photofragments

The observed TOF spectra of the Cl fragments at $m/z=35$ are shown at several scattering angles, Θ, in Figs. 4(a)–4(c). The data are represented by the open circles, while the solid and dashed lines are the results of forward-convolution simulations of the experiment using optimized center-of-mass translational energy distributions shown in Fig. 5.

As has been briefly discussed in the previous letter,[4] we note that a bimodal $P(E_T)$ distribution for the $Cl+N_3$ channel is needed to fit the two dominant peaks in the TOF spectra of Figs. 4(a)–4(c). The individual contributions are shown as dashed (fast channel) and solid lines (slow channel), respectively. The $P(E_T)$ distribution for the Cl data in Fig. 5 is experimentally indistinguishable from that obtained by Hansen and Wodtke in a recent velocity map imaging experiment, in which the faster feature was assigned to the formation of linear N_3 and the slower feature was interpreted as possible evidence for the photolytic production of cyclic N_3.[1] Thus, the photofragment translational spectroscopy experiment confirms the existence of a bimodal Cl-atom translational energy distribution in the radical channel. The anisotropy parameters are determined to be $\beta=1.75(10)$ and $\beta=0.35(5)$ for the fast and slow channels, respectively. Those values compare well with those determined by velocity map imaging [$\beta=1.70(5)$ and $\beta=0.39(1)$].[1] The branching ratio between the two channels is fast Cl/slow Cl ~0.75/0.25. Using the velocity map imaging technique a similar branching ratio of 0.8/0.2 was found.[1] The $P(E_T)$ distribution shown in Ref. 4 exhibiting more of the slow channel is incorrect.

A closer look at the TOF spectra of the Cl product in Fig. 4 indicates a small contribution from very fast photofragments. This feature is most obvious at larger scattering angles and it is shown as dotted curve enlarged in the inset of Fig. 4(c) for the $\Theta=50°$ data. This feature results from secondary photodissociation of NCl at 248 nm:

$$NCl(X\,^3\Sigma, a\,^1\Delta) + h\nu \rightarrow N(^4S, ^2D) + Cl(^2P). \quad (7)$$

The derived $P(E_T)$ for the secondary photodissociation of NCl peaks at 80 kcal/mol and exhibits a half-width of ~10 kcal/mol. In principle, we can use this information to evaluate the internal energy content of the NCl photodisso-

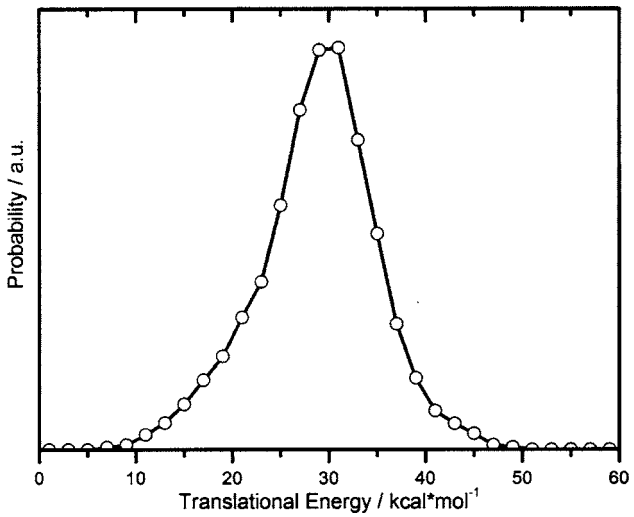

FIG. 3. Center-of-mass translational energy distribution $P(E_T)$ for the molecular channel forming NCl in the ClN_3 photodissociation. This energy distribution is used to reproduce the observed spectra in Fig. 2.

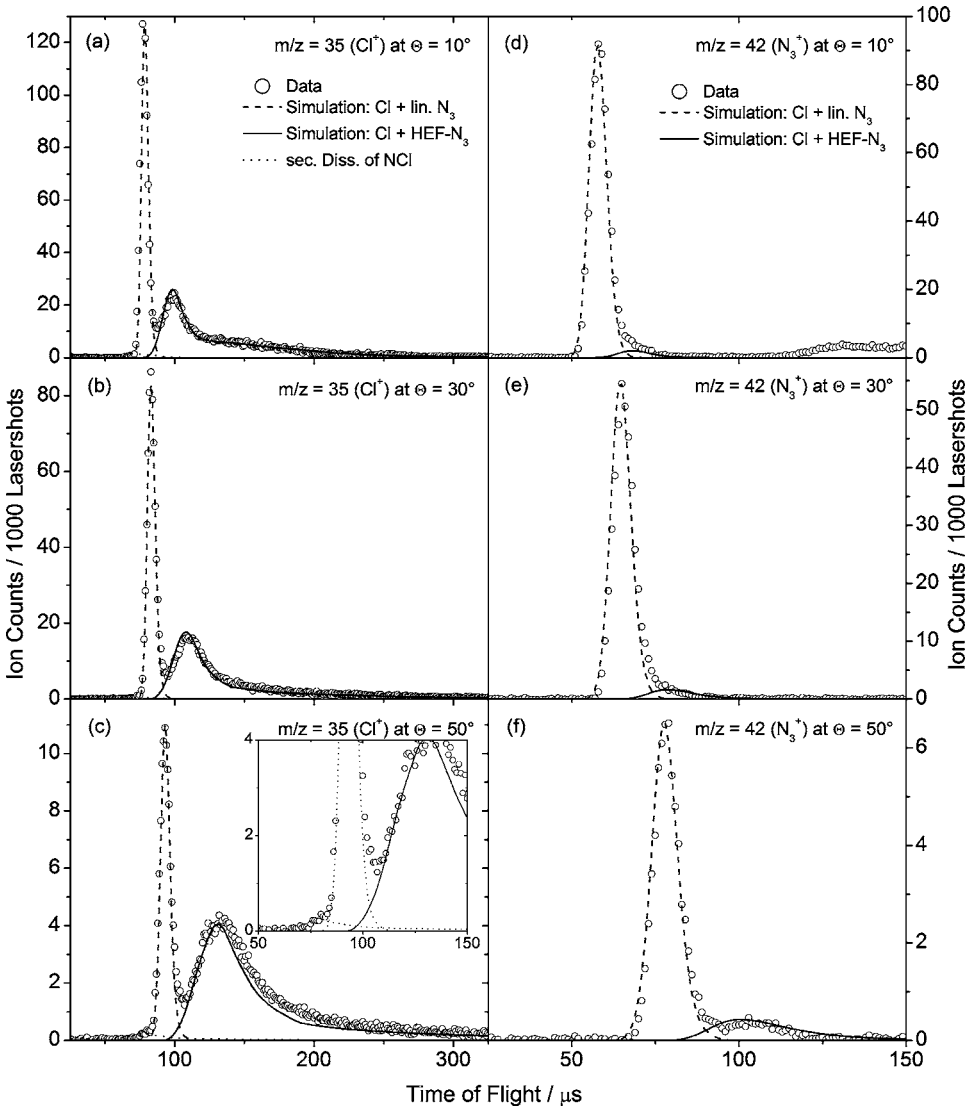

FIG. 4. (a)–(c) TOF spectra of $m/z=35(Cl^+)$ and (d)–(f) TOF spectra of $m/z=42(N_3^+)$ at detection angles $\Theta=10°$, 30°, and 50°. For all spectra the open circles represent the data. The dashed lines represent the forward-convolution fit to the data using the $P(E_T)$ distribution shown in Fig. 5 of the "fast" linear-$N_3(X\,^2\Pi)$ forming channel. The solid lines represent the "slow" N_3 forming channel. In (a)–(c) an additional contribution from secondary photodissociation of NCl photofragments can be seen, especially in the inlet in (c) as dotted line.

ciated in this work. In practice, this analysis is ambiguous, as the identities of the reactant and product electronic states in (7) are not known.

N_3 *photofragments*

The observed TOF spectra of the N_3 counterfragment for radical channel (2) are shown in Figs. 4(d)–4(f). Again, the data are represented by the open circles, the simulations by the dashed (fast channel) and solid (slow channel) lines. As will be discussed below, the strongest peak in the N_3 TOF spectra corresponds to the formation of linear azide. However, a second peak which is much more obvious in the Cl^+ data is—in part—also present.

The N_3 TOF spectra shown in Figs. 4(d)–4(f) were used to derive a center-of-mass translational energy distribution for the radical channel, similar to what was done for the Cl TOF data. The results of this analysis are shown in Fig. 5 and are compared to the $P(E_T)$ obtained from the analysis of the Cl data. The derived translational energy distributions match closely above about 26 ± 2 kcal/mol. This suggests that while low-translational energy Cl atoms formed together with HEF-N_3 can easily be detected at the ionizer after about 100 μs, not all of the corresponding HEF-N_3 can. Comparing the intensities of the slow channels in Fig. 5 we conclude that 10% of the HEF-N_3 fragments are actually detected. This could be due to the preferential ion fragmentation possible for highly energized neutrals or to the onset of unimolecular dissociation of the neutral N_3 on a time scale faster than 100 μs. It could also be due to secondary photodissociation of N_3, if the internal energy of the N_3 were to have a strong influence on the photodissociation cross section of the molecule at 248 nm.

In addition to yielding a $P(E_T)$ distribution, the $m/z=42(N_3^+)$ TOF data allowed us to determine the anisotropy parameters for the reactions (2a) and (2b) by way of an independent set of data. The derived values of $\beta=1.7(1)$ and $\beta=0.39(5)$ for reactions (2a) and (2b), respectively, agree with results obtained by analyzing angular distribution of the Cl fragments by both photofragment translational spectroscopy and velocity map imaging. The correspondence between β parameters and translational energy distributions indicates that both the fast and the slow channel in the Cl data are indeed correlated to the formation of momentum-matched N_3 counterfragments. This shows clearly that besides the linear N_3, HEF-N_3 is formed and can be detected by EI mass spectrometry.

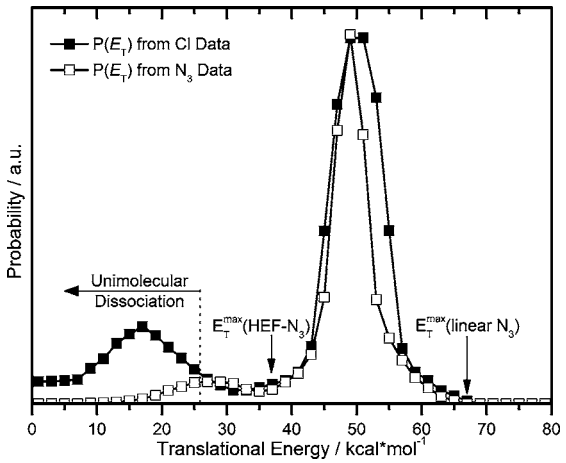

FIG. 5. Center-of-mass translational energy distributions $P(E_T)$ for the radical channel forming N_3+Cl in the ClN_3 photodissociation. One $P(E_T)$ is derived from the analysis of the Cl TOF spectra measured at six different scattering angles Θ, partially shown in Figs. 4(a)–4(c). A similar $P(E_T)$ is derived from the N_3 TOF data set which are partially shown in Figs. 4(d)–4(f). The shown energy distributions are able to produce the fit to all of the TOF data shown in Fig. 4.

The observed translational energy distributions are quantitatively consistent with the formation of linear N_3. The dissociation energy of ClN_3 to form Cl and linear N_3 is $D_0(\text{Cl–N}_3)=49.1$ kcal/mol.[1,29] If all the available energy is channeled into translational energy, i.e., the products are formed in their ground states, the maximum translational energy release would be 66.1 kcal/mol, using a photon energy of 115 kcal/mol ($\lambda=248$ nm). The observed maximum translational energy release $[E_T{}^{\max}(\text{linear N}_3+\text{Cl})=66.9\pm1$ kcal/mol] is marked in Fig. 5 and agrees well with the predicted value. We therefore assign the fast Cl and N_3 fragments to the formation of linear N_3 in reaction (2a). This assignment is supported by another experiment by Samartzis *et al.* who determined the ionization potential of the fast N_3 fragments to IP=11.1 eV which can be identified with the well-known IP of linear N_3.[5,37]

For the slow Cl+N_3 channel, the maximum observed translational energy release is $E_T{}^{\max}(\text{HEF-N}_3+\text{Cl})=36.8\pm2$ kcal/mol (see Fig. 5), a value which is derived from the Cl as well as the N_3 data. The difference between the maximum translational energy release of the fast and slow channels represents the excitation energy of HEF-N_3 with respect to ground-state linear N_3. This value (30.1±3 kcal/mol) agrees well with a previous experimentally determined excitation energy (31±2 kcal/mol) obtained from velocity maps of the Cl fragments.[1]

Secondary dissociation processes: N_2^+ and N^+ data

As mentioned above, comparison of the TOF spectra in Fig. 4 and the translational energy distributions in Fig. 5 leads to the conclusion that only 10% of the slow N_3 photofragments are detected. Consequently we looked at the TOF spectra for $m/z=14(N^+)$ and $m/z=28(N_2^+)$ for evidence of unimolecular and/or photoinduced dissociation of N_3.

The data are shown in Figs. 6 and 7 for different scattering angles, Θ. The data are represented by the open circles

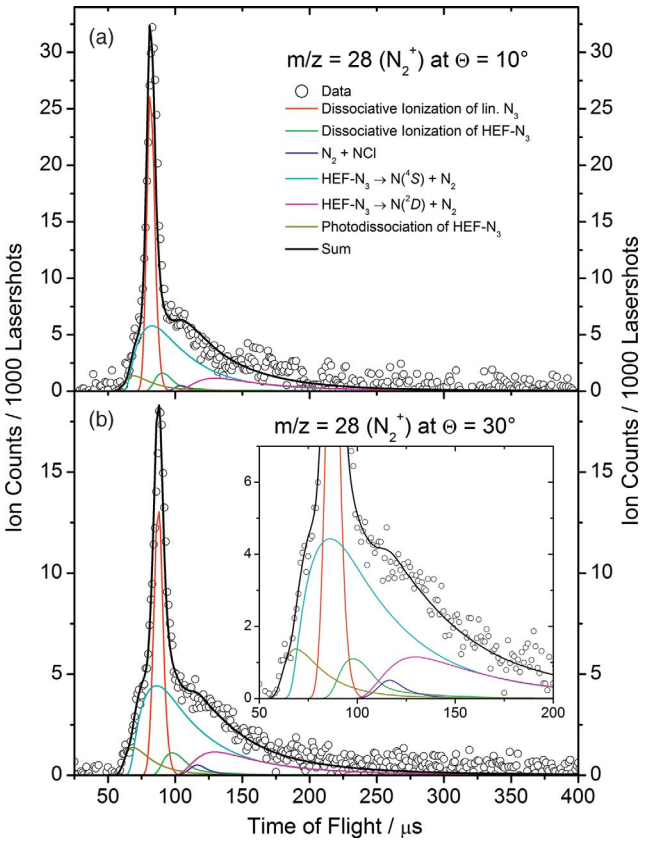

FIG. 6. (Color) TOF spectra of $m/z=28(N_2^+)$ at detection angles $\Theta=10°$ and 30°. For both spectra the open circles represent the data. A strong peak is clearly visible in all TOF spectra which is believed to arise from dissociative ionization of linear N_3 in the ion source (red line). All minor features which are shown enlarged in the embedded window in (b) are simulated by taking the dissociative ionization of HEF-N_3 (green), the unimolecular dissociation (cyan and magenta), and the photodissociation (dark yellow) of HEF-N_3 into $N_2+N(^4S,{}^2D)$, and of course the primary molecular N_2+NCl channel (blue) into account.

and the simulations which will be discussed in this section are represented by the colored lines. Because of the molecular channel forming N_2 being just a minor channel[4] (5±3%) and because of the high background and low S/N experienced (due to background CO in the detector), for $m/z=28$ we were limited to obtaining data at $\Theta=10°$ and 30°.

Dissociative ionization of N_3 *photofragments*

Figures 6 and 7 show that both the $m/z=14$ and the $m/z=28$ TOF spectra are dominated by a strong peak which, when corrected for differences in ion flight through the quadrupole mass spectrometer, appears at the same TOF as the dominant peak in the $m/z=42$ TOF data, now assigned to the formation of the linear $N_3(X\,{}^2\Pi)$. It is therefore clear that the major peaks in the $m/z=14(N^+)$ and $28(N_2^+)$ data result from dissociative ionization of linear N_3 in the ionizer and provide redundant information on reaction (2a). Since EI with electron energies of ~160 eV was used, observing ionizer-induced fragmentation is not surprising. Because it is energetically more favorable and therefore, on the basis of statistical theories of ion dissociation more likely for N_3^+ to

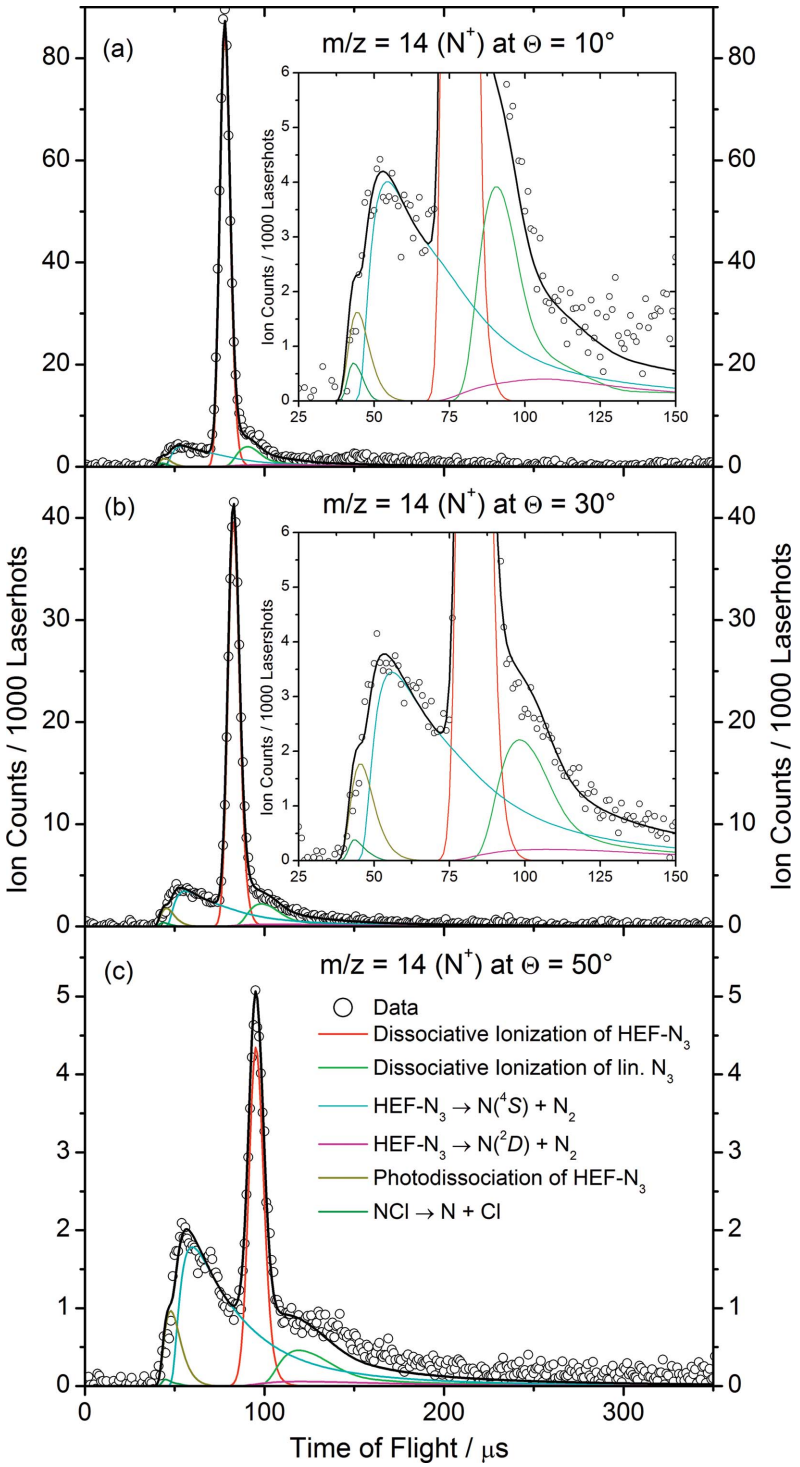

FIG. 7. (Color) TOF spectra of $m/z=14(N^+)$ at detection angles $\Theta=10°$, 30°, and 50°. For all shown spectra the open circles represent the data. A strong peak is clearly visible in all TOF spectra which is believed to arise from dissociative ionization of linear N_3 in the ion source. To simulate all observed features which are shown enlarged in the inlets of (a) and (b) a total of six channels was included: dissociative ionization of linear (red) and HEF-N_3 (green), the unimolecular dissociation of HEF-N_3 fragments into $N_2+N(^4S)$ (cyan) and $N_2+N(^2D)$ (magenta) was considered. The fastest flying N fragments derive from secondary photodissociation of N_3 (dark yellow) and NCl fragments (olive). The legend is shown in (c).

dissociate into N_2+N^+ rather than into N_2^++N, this feature is substantially stronger in the $m/z=14$ than in the $m/z=28$ TOF spectra.

Besides evidence for linear N_3 observed after dissociative ionization, there are additional features clearly visible in the $m/z=28(N_2^+)$ and $m/z=14(N^+)$ TOF spectra in Figs. 6 and 7. To simulate the observed spectra, several pathways had to be included. Information about some of these channels is already in hand. For example, if the linear-N_3 fragment dissociates in the ionizer due to electron impact, it is safe to assume that the less stable HEF-N_3 will dissociate as well. To include those secondary fragmentation processes, the translational energy distributions which are shown in Fig. 5 and the anisotropy parameters for both the fast and slow N_3 channels were used as input parameters without any additional modifications. In Figs. 6 and 7 their contribution to the signal is shown using red and green lines for the fragmentation of the fast N_3 and slow N_3, respectively.

Unimolecular dissociation of HEF-N_3

While this analysis assumes the fragmentation pattern of linear and HEF-N_3 to be similar, no amount of adjustment of the relative contributions of the slow and fast radical chan-

nels can reproduce the $m/z=28$ and $m/z=14$ data. In particular, the fastest appearing signal is far too translationally excited to be accounted for by either of these reactions. There is also signal in these TOF spectra that appears somewhat slower than would be expected. In the $m/z=28(N_2^+)$ TOF data, some of this is due to the molecular channel (blue), but this cannot explain the TOF quantitatively.

As pointed out earlier, the comparison of the observed $m/z=35(Cl^+)$ and the $m/z=42(N_3^+)$ TOF spectra and the corresponding translational energy distributions suggests that HEF-N_3 fragments with $E_{int} \geqslant 11 \pm 2$ kcal/mol (above the ground state of the HEF-N_3 isomer) undergo unimolecular dissociation, for example,

$$N_3^* \rightarrow N_2(X\,^1\Sigma_g^+) + N(^4S). \tag{8}$$

For N_3 molecules with enough internal energy, reaction (8) can provide a substantial translational energy release. The contribution from this channel is shown (cyan) in Figs. 6 and 7.

Photodissociating ClN_3 at $\lambda=248$ nm ($h\nu=115$ kcal/mol) may form N_3 with enough internal energies to dissociate by the spin-allowed reaction,

$$N_3^* \rightarrow N_2(X\,^1\Sigma_g^+) + N(^2D). \tag{9}$$

Product flux through this channel releases much less translational energy, as a great deal of the available energy is converted to N-atom electronic excitation. The contribution of this channel to the $m/z=28(N_2^+)$ and the $m/z=14(N^+)$ TOF spectra can be seen as magenta lines in Figs. 6 and 7, respectively.

To simulate these secondary processes, the translational energy distribution of the N_3 molecules dissociating through reaction (8) was found by taking the difference between the two $P(E_T)$'s shown in Fig. 5. This calculated translational energy distribution is used to model the laboratory flux of N_3 molecules that go on to dissociate. The previously described forward-convolution program[35] then uses a "secondary" $P(E_T)$ characterizing the translational energy release of reaction (8) to calculate the laboratory flux and the TOF spectra for N and N_2. The secondary $P(E_T)$ was iteratively adjusted to obtain the best fit. The same strategy was used to account for the N_3 molecules that undergo reaction (9). However, here the translation energy distribution of the dissociating N_3 molecules was assumed to be the product of the $P(E_T)$ distribution for the Cl atom and a heavy-side step function at $E_T=12$ kcal/mol, scaled to best fit the data.

Photodissociation of N_3

Including the unimolecular dissociation of HEF-N_3 is clearly necessary to fit the $m/z=14$ and 28 data. However, as can be seen in Fig. 6, especially in the inset in Fig. 6(b), none of the channels mentioned so far accounts for the fastest N_2 fragments. The fastest fragments can only be formed by a two-photon process, i.e., by secondary photodissociation of primary N_3 fragments. Consequently, an additional channel was included in the analysis simulating the photodissociation of N_3 fragments:

$$N_3 + h\nu \rightarrow N_2(X\,^1\Sigma_g^+) + N(^2D). \tag{10}$$

A thorough analysis, summarized in Figs. 8 and 9, was undertaken which attempted to model the data using photodissociation of either HEF- or linear N_3. Figure 8 shows the $m/z=28$ and $m/z=14$ TOF spectra for $\Theta=30°$. The first row shows the best fits obtained to the data if one neglects secondary photodissociation of N_3 altogether. Although it is possible to fit the N^+ data, due the presence of the fast moving N atoms from NCl photodissociation, it is clear that the fastest N_2 fragments are not accounted for in this model.

This fast signal can be fitted assuming secondary photodissociation of N_3, as shown in the second row of spectra in Fig. 8. The data were fitted equally well using either of the two secondary $P(E_T)$ distributions in Fig. 9 and an anisotropy parameter $\beta=0.7$. The slower distribution in Fig. 8 assumes that the primary products are fast $Cl+N_3$, i.e., linear N_3 is dissociated by a second photon, while the faster distribution assumes the primary products to be slow $Cl+N_3$, with HEF-N_3 undergoing secondary dissociation. The fits to the data alone cannot distinguish these two possibilities. However, the vertical arrows in Fig. 9 show the maximum E_T values, E_T^{max}, thermodynamically allowed from secondary photodissociation of linear and HEF-N_3, using the average value of the fast and slow Cl fragments (30 and 9 kcal/mol, respectively) to specify the N_3 internal energy. We find that E_T^{max} for HEF-N_3 matches the maximum in the secondary $P(E_T)$ distribution assuming photodissociation of HEF-N_3, whereas E_T^{max} for linear N_3 lies considerably beyond the maximum of the corresponding secondary $P(E_T)$ distribution. Figure 9 thus offers indirect evidence that most of the secondary photodissociation signal is from HEF-N_3.

Overall fits to the N_2^+ *and* N^+ *data*

In addition to the already described processes (dissociative ionization, unimolecular dissociation, and secondary photodissociation of N_3 photofragments) the primary molecular channel (1) had to be included in a complete analysis of the $m/z=28(N_2^+)$ TOF spectra. Because of the branching ratios of 95%/5% in favor of the radical channel, the contribution of the molecular channel forming N_2 and NCl is limited.[4] The primary translational energy distribution shown in Fig. 3 was used without any changes and the respective contribution is shown as blue line in Fig. 6 and it is clearly visible that all six individual contributions add up nicely to fit the observed data.

The secondary photodissociation of NCl photoproducts was observed in the $m/z=35$ TOF spectra and therefore reaction (7) had to be included in the analysis of the $m/z=14(N^+)$ data. NCl photodissociation was modeled using the secondary $P(E_T)$ used to simulate the $m/z=35$ data and an anisotropy parameter $\beta=1.1$, indicating a parallel transition. The contributions from all described channels to the overall observed $m/z=14$ signal are shown in Fig. 7.

DISCUSSION

The results presented above show that the fast and slow Cl fragments are correlated to the formation of linear N_3 and

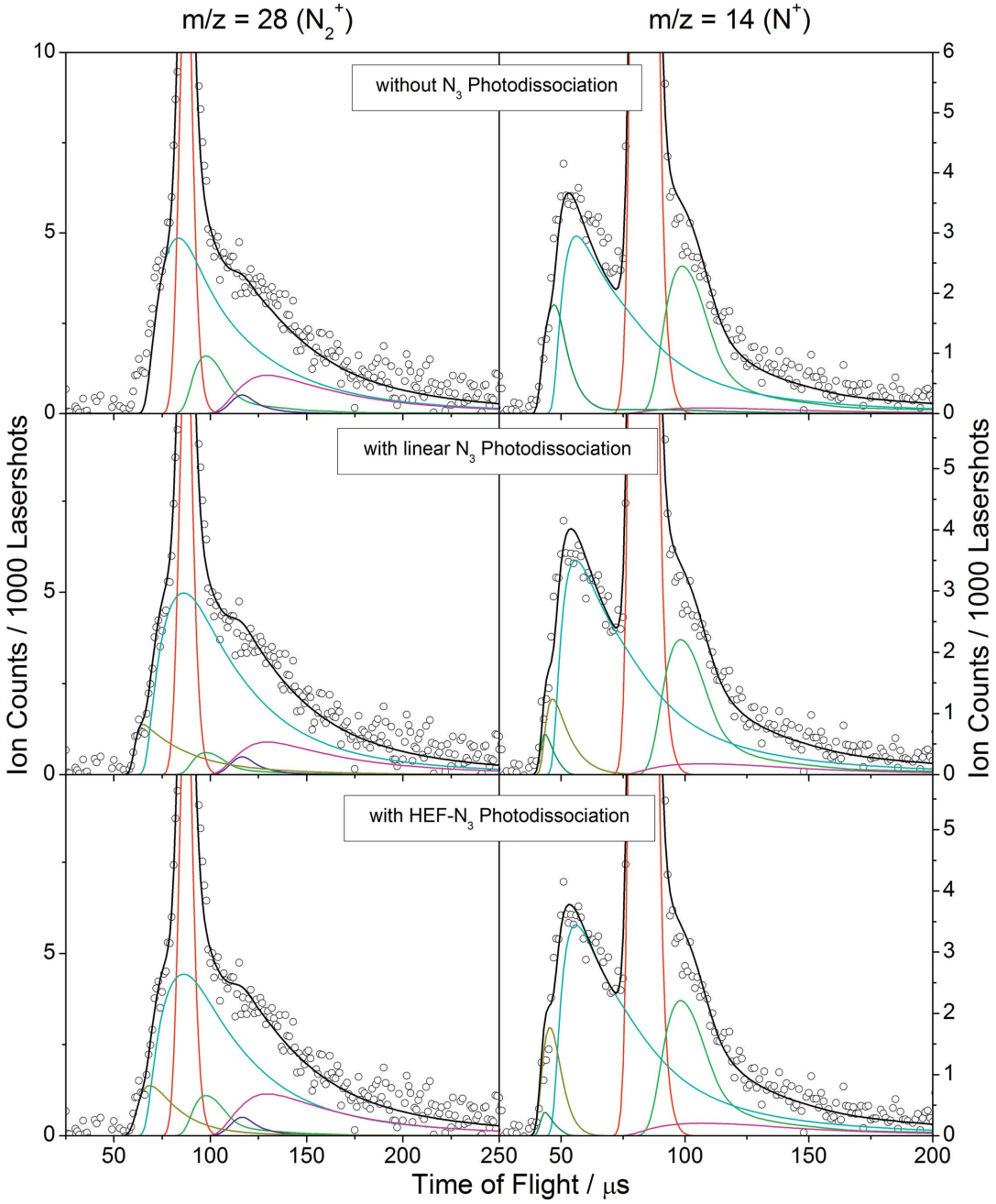

FIG. 8. (Color) Time-of-flight spectra taken at $\Theta=30°$ for $m/z=28(N_2^+)$ (left column) and $m/z=14(N^+)$ (right column). The first row shows the best fits excluding any secondary photodissociation processes of N_3 fragments. The second and third rows show the best fit including photodissociation of linear and HEF-N_3 isomers, respectively. Each contribution is shown in the same color as in Figs. 6 and 7.

HEF-N_3, respectively. The observed excitation energy of HEF-N_3 $\Delta E=30.1\pm3$ kcal/mol agrees well with a previously determined excitation energy 31 ± 2 kcal/mol obtained from velocity maps of the Cl fragments at a somewhat different photolysis wavelength ($\lambda=235$ nm).[1] We now have two experiments with different product detection methods at two different wavelengths that both lead to a quantitatively indistinguishable heat of formation for the HEF-N_3. This adds further weight to the interpretation of the bimodal energy distribution as two isomers as opposed to a bimodal vibrational energy distribution of linear N_3. These experimental determinations are consistent with theoretical predictions of the heat of formation of the cyclic-N_3 isomer. Bittererova *et al.* calculated the excitation energy of cyclic N_3 to be 30.0 kcal/mol, in excellent agreement with these results[23] and with results from Zhang *et al.* who calculated an energy difference of 30.3 kcal/mol.[25] Although other explanations of the observed bimodal translational energy distributions still cannot be ruled out, this simple energy consideration shows that all experiments carried out so far on ClN_3 photodissociation under collision-free conditions are consistent with photolytic formation of cyclic N_3.

However, the data also indicate that N_3 isomers with internal energies of $E_{int}\geqslant 11\pm2$ kcal/mol (with respect to the cyclic-N_3 minimum) undergo rapid unimolecular dissociation and therefore cannot be detected by our present experi-

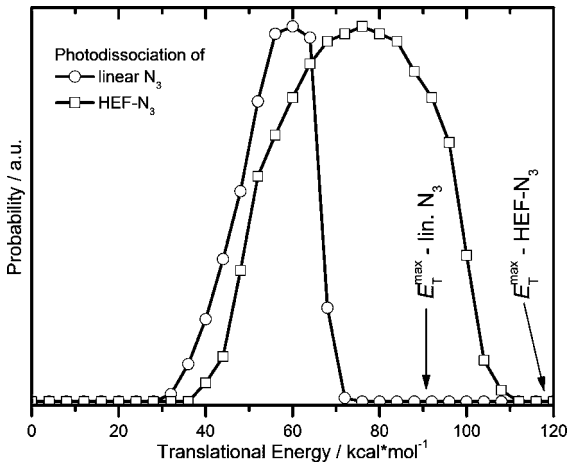

FIG. 9. Secondary translational energy distributions for the N_3 photodissociation process which fits best the data shown in Fig. 8. The secondary $P(E_T)$ after dissociating linear N_3 is shown to the left. The cutoff at 72 kcal/mol does not match the predictions of ~91 kcal/mol. The secondary $P(E_T)$ after dissociating the HEF-N_3 isomer is shown on the right. The cutoff at 116 kcal/mol matches well with the prediction of 118 kcal/mol.

mental setup. Recently, Babikov *et al.* published a comprehensive study of the unimolecular dissociation of the N_3 radical on the ground doublet and excited quartet potential-energy surfaces based on multireference single and double excitation configuration interaction and second-order multireference perturbation methods. The calculations, which do not include the influence of the geometric phase effect, suggest that the doublet-quartet surface crossings that lead to dissociation lie between 17 and 30 kcal/mol above the cyclic-N_3 minimum.[19] In Fig. 1 the observed threshold for dissociation (gray bar) is compared with the calculated thresholds and doublet-quartet seam crossings. Present theory does not allow us to understand the apparent dissociation threshold at 11 kcal/mol. Further theoretical work incorporating the geometric phase effect's influence into doublet-quartet seam crossings may be necessary to resolve this discrepancy. It should be pointed out that some HEF-N_3 is detected even when containing internal energies that exceed the doublet-quartet seam crossing calculated by theory.

The fact that the secondary dissociation products, N and N_2, were detected and the corresponding TOF spectra could be analyzed successfully taking into account the unimolecular dissociation and secondary photodissociation of HEF-N_3 provides further support for the photochemical mechanism derived from this work.

The possibility that the observed slow Cl channel arises from unimolecular dissociation of excited NCl fragments can be ruled out for several reasons. In a previous letter, it was shown that N_2+NCl is a minor channel ($5\pm3\%$) compared to the radical-forming N_3+Cl channel ($95\pm3\%$).[4] Even if we would assume that N_2+NCl is the main product and that it is because of the unimolecular dissociation of excited NCl primary photoproducts that not all of the NCl is detected, we still would miss the N_2 and N counterfragments in the $m/z=28$ and $m/z=14$ TOF spectra. The dominant peak in the $m/z=28(N_2^+)$ data appears at the same time as the strongest peak in the $m/z=42(N_3^+)$ and the $m/z=14(N^+)$ data. The only reasonable explanation is dissociative ionization of the linear-N_3 fragment in the ionizing region of the mass spectrometer. Therefore we confirm the previous analysis of N_2 +NCl being a minor channel and that slow Cl fragments are actually formed by reaction (2a) and (2b).

CONCLUSIONS

We performed photofragment translational spectroscopy experiments to reveal the primary and secondary decomposition pathways of chlorine azide, ClN_3, when photolyzed at $\lambda=248$ nm. Special attention is paid to the radical channel (2a) and (2b) forming Cl+N_3 and the following secondary unimolecular dissociation and photodissociation processes of highly excited N_3 fragments.

Bimodal translational energy distributions for both the Cl and the N_3 fragments clearly show that two distinct forms of the N_3 radical are produced. Besides the formation of the ground-state (linear azide) N_3 radical a *high-energy form* (HEF) of N_3 (possible cyclic N_3) is formed.

The observed energy difference between the linear N_3 and the HEF-N_3 isomer of $\Delta E=30.1\pm3$ kcal/mol agrees well with calculations performed by Bittererova *et al.*[23] and previous velocity map imaging experiments at a different photolysis wavelength.[1]

Both forms of N_3 were detected by electron-impact ionization. A lower limit of the lifetime of the HEF-N_3 was determined to be $\tau\geqslant100$ μs.

N_3 fragments with more than 11 ± 2 kcal/mol of internal energy above the cyclic-N_3 minimum appear to undergo unimolecular decomposition or photodissociation. The secondary N_2 and N unimolecular dissociation fragments were detected and the observed translational energy distributions of those products were successfully interpreted by a chemical model where highly excited N_3 radicals fragment into both $N_2(X\,^1\Sigma_g^+)$+N(^4S) and $N_2(X\,^1\Sigma_g^+)$+N(^2D). The fastest observed N and N_2 fragments are produced by secondary photodissociation processes of the primary NCl and N_3 photoproducts. There is indirect evidence that HEF-N_3 is selectively photodissociated at 248 nm in the presence of linear azide.

The observed translational energy releases of both the N and N_2 fragments cannot be explained by unimolecular decomposition of energized NCl fragments. Therefore, we rule this secondary process out as a source of the observed slow Cl fragments.

In summary, the velocity map imaging and the photofragment translational spectroscopy experiment carried out so far on this molecule are consistent with photolytic formation of cyclic N_3—although the structure of the HEF-N_3 species remains unclear and more work is needed.

ACKNOWLEDGMENTS

One of the authors (A.M.W.) acknowledges the support of an Air Force Office of Scientific Research contract under Grant No. F49620-95-1-0234. Another author (N.H.) acknowledges the support of the Alexander von Humboldt-Foundation under a Fyodor-Lynen Stipend while working at UCSB. One of the authors (D.M.N.) acknowledges support from the Air Force Office of Scientific Research under Grant

No. F49620-03-1-0085. Sandia is a multiprogram laboratory operated by Sandia Corporation, a Lockheed Martin Company, for the US Department of Energy's National Nuclear Security Administration under Contract No. DE-AC04-94-AL85000.

[1] N. Hansen and A. M. Wodtke, J. Phys. Chem. A **107**, 10608 (2003).
[2] N. Hansen, A. M. Wodtke, A. V. Komissarov, and M. C. Heaven, Chem. Phys. Lett. **368**, 568 (2003).
[3] N. Hansen, A. M. Wodtke, A. V. Komissarov, K. Morokuma, and M. C. Heaven, J. Chem. Phys. **118**, 10485 (2003).
[4] A. M. Wodtke, N. Hansen, J. C. Robinson, N. E. Sveum, S. J. Goncher, and D. M. Neumark, Chem. Phys. Lett. **391**, 334 (2004).
[5] P. C. Samartzis, J. J. Lin, T. Ching, C. Chadhuri, Y. T. Lee, S. Lee, and A. M. Wodtke J. Chem. Phys. **123**, 051101 (2005).
[6] R. D. Coombe, D. Patel, A. T. Pritt, and F. J. Wodarczyk, J. Chem. Phys. **75**, 2177 (1981).
[7] A. J. Ray and R. D. Coombe, J. Phys. Chem. **97**, 3475 (1993).
[8] A. J. Ray and R. D. Coombe, J. Phys. Chem. **98**, 8940 (1994).
[9] T. L. Henshaw, S. D. Herrera, G. W. Haggquist, and L. A. V. Schlie, J. Phys. Chem. A **101**, 4048 (1997).
[10] R. H. Jensen, A. Mann, and R. D. Coombe, J. Phys. Chem. A **104**, 6573 (2000).
[11] A. V. Komissarov, G. C. Manke, S. J. Davis, and M. C. Heaven, J. Phys. Chem. A **106**, 8427 (2002).
[12] R. D. Coombe, S. J. David, T. L. Henshaw, and D. J. May, Chem. Phys. Lett. **120**, 433 (1985).
[13] S. P. Tinney, J. Han, and M. C. Heaven, Proc. SPIE **5334**, 25 (2004).
[14] T. L. Henshaw, G. C. Manke, T. J. Madden, M. R. Berman, and G. D. Hager, Chem. Phys. Lett. **325**, 537 (2000).
[15] G. C. Manke and G. D. Hager, J. Mod. Opt. **49**, 465 (2002).
[16] A. J. Ray and R. D. Coombe, J. Phys. Chem. **99**, 7849 (1995).
[17] J. M. Herbelin, T. L. Henshaw, B. D. Rafferty, B. T. Anderson, R. F. Tate, T. J. Madden, G. C. Manke, and G. D. Hager, Chem. Phys. Lett. **299**, 583 (1999).
[18] G. C. Manke, C. B. Cooper, S. C. Dass, T. J. Madden, and G. D. Hager, IEEE J. Quantum Electron. **39**, 995 (2003).
[19] D. Babikov, P. Zhang, and K. Morokuma, J. Chem. Phys. **121**, 6743 (2004).
[20] D. Babikov, B. K. Kendrick, P. Zhang, and K. Morokuma, J. Chem. Phys. **122**, 044315 (2005).
[21] R. Resta, J. Phys.: Condens. Matter **12**, R107 (2000).
[22] M. V. Berry, Proc. R. Soc. London, Ser. A **392**, 45 (1984).
[23] M. Bittererova, H. Ostmark, and T. Brinck, J. Chem. Phys. **116**, 9740 (2002).
[24] R. Tarroni and P. Tosi, Chem. Phys. Lett. **389**, 274 (2004).
[25] P. Zhang, K. Morokuma, and A. M. Wodtke, J. Chem. Phys. **122**, 014106 (2005).
[26] J. M. L. Martin, J. P. Francois, and R. Gijbels, J. Chem. Phys. **93**, 4485 (1990).
[27] R. E. Continetti, D. R. Cyr, D. L. Osborn, D. J. Leahy, and D. M. Neumark, J. Chem. Phys. **99**, 2616 (1993).
[28] C. Paillard, R. Moreau, and J. Combouri, C. R. Seances Acad. Sci., Ser. C **264**, 1721 (1967).
[29] M. Otto, S. D. Lotz, and G. Frenking, Inorg. Chem. **31**, 3647 (1992).
[30] S. S. Xantheas, T. H. Dunning, and A. Mavridis, J. Chem. Phys. **106**, 3280 (1997).
[31] Y. T. Lee, J. D. McDonald, P. R. Lebreton, and D. R. Herschbach, Rev. Sci. Instrum. **40**, 1402 (1969).
[32] J. C. Robinson, S. A. Harris, W. Z. Sun, N. E. Sveum, and D. M. Neumark, J. Am. Chem. Soc. **124**, 10211 (2002).
[33] D. Proch and T. Trickl, Rev. Sci. Instrum. **60**, 713 (1989).
[34] S. A. Harich, PHOTRAN, a program for forward convolution analysis of photodissociation, 2003.
[35] A. M. Wodtke, ANALMAX, forward convolution analysis of photodissociation including secondary processes, 2004.
[36] A. T. Pritt, D. Patel, and R. D. Coombe, J. Chem. Phys. **75**, 5720 (1981).
[37] J. M. Dyke, N. B. H. Jonathan, A. E. Lews, and A. Morris, Mol. Phys. **47**, 1231 (1982).